Trabid patient mutations impede the axonal trafficking of adenomatous polyposis coli to disrupt neurite growth

Daniel Frank[1,7,14], Maria Bergamasco[2,7,14], Michael Mlodzianoski[3,7,14], Andrew Kueh[4,7,8,9], Ellen Tsui[5,7], Cathrine Hall[6,7], Georgios Kastrappis[10], Anne Kathrin Voss[2,7], Catriona McLean[11], Maree Faux[12], Kelly Rogers[3,7], Bang Tran[10], Elizabeth Vincan[10,13], David Komander[1,7], Grant Dewson[1,7,15], and Hoanh Tran[1,7,10,15]

[1]Ubiquitin Signalling Division, [2]Epigenetics and Development Division, [3]Centre for Dynamic Imaging, [4]Melbourne Advanced Genome Editing Centre, [5]Histology Facility, [6]Inflammation Division, Walter and Eliza Hall Institute of Medical Research, Parkville, VIC 3052, Australia
[7]Department of Medical Biology, The University of Melbourne, Parkville, VIC 3052, Australia
[8]Olivia Newton-John Cancer Research Institute, Heidelberg, VIC 3084, Australia
[9]School of Cancer Medicine, La Trobe University, Heidelberg, VIC 3084, Australia
[10]Department of Infectious Diseases, The University of Melbourne at The Peter Doherty Institute for Infection and Immunity, Melbourne, VIC 3000, Australia
[11]Department of Anatomical Pathology, The Alfred Hospital, Melbourne, VIC 3004, Australia
[12]Neuro-Oncology Group, Murdoch Children's Research Institute, Parkville, VIC 3052, Australia
[13]The Victorian Infectious Diseases Reference Laboratory, Royal Melbourne Hospital at The Peter Doherty Institute for Infection and Immunity, Melbourne, VIC 3000, Australia
[14]These authors contributed equally to this work
[15]Corresponding authors dewson@wehi.edu.au, tran.h@wehi.edu.au

Running Title: Deubiquitylating enzyme Trabid controls polarised axon elongation

Abstract

Trabid/ZRANB1 missense mutations have been identified in children diagnosed with a range of congenital disorders including reduced brain size, but how Trabid regulates neurodevelopment is not understood. We have characterised these patient mutations in cells and mice to identify a key role for Trabid in the regulation of neurite growth. One of the patient mutations flanked the catalytic cysteine of Trabid and its deubiquitylating (DUB) activity was abrogated. The second variant retained DUB activity, but failed to bind STRIPAK, a large multiprotein assembly implicated in cytoskeleton organisation and neural development. *Trabid/ZRANB1* knock-in mice harbouring either of these patient mutations exhibited reduced neuronal and glial cell densities in the brain and a motor deficit consistent with fewer dopaminergic neurons and projections. Mechanistically, both DUB-impaired and STRIPAK-binding-deficient Trabid variants impeded the trafficking of adenomatous polyposis coli (APC) to microtubule plus-ends. Consequently, the formation of neuronal growth cones and the trajectory of neurite outgrowth from mutant midbrain progenitors were severely compromised. We propose that STRIPAK recruits Trabid to deubiquitylate APC, and that in cells with mutant Trabid, APC becomes hyperubiquitylated and mislocalised causing impaired organisation of the cytoskeleton that underlie the neuronal and developmental phenotypes.

Introduction

Deubiquitylating enzymes (DUBs) are integral components of the ubiquitin system that control protein functions essential for healthy development and aging (Clague et al. 2019). DUBs catalyze the removal of ubiquitin from protein substrates to regulate protein stability, activity, interaction, or localisation (Komander et al. 2009). Ubiquitin can be assembled into polymers linked through one of eight internal ubiquitin residues – Met1, Lys6, Lys11, Lys27, Lys29, Lys33, Lys48 and Lys63 – and impairment of DUB function can lead to the accumulation of one or more of these ubiquitin chain linkages on a protein substrate with deleterious consequences. For example, LINKage-specific deubiquitylation deficiency-induced Embryonic Defects (LINKED), a human syndrome caused by loss-of-function mutations in the DUB OTUD5, is associated with increased Lys48-linked ubiquitylation and turnover of chromatin remodeling and transcription factors that are critical for normal embryonic development (Beck et al. 2021).

Consequently, LINKED syndrome patients manifest severe congenital malformations and die in early infancy (Beck et al. 2021). OTUD5 belongs to a 17-member family of human DUBs that possess an OTU (*o*varian *tu*mour) catalytic domain and include the closely related OTU DUBs A20, Cezanne and Trabid. Trabid missense mutations have been identified in children diagnosed with a range of developmental disorders including microcephaly (Deciphering Developmental Disorders 2015).

Trabid has two defining biochemical features. First, it exhibits strong DUB specificity for Lys29- and Lys33-linked ubiquitin chains, cleaving these chain types 40-fold more efficiently than Lys63-linked chains (Licchesi et al. 2012). Lys29-linked polyubiquitin exists mainly as heterotypic chains containing Lys48 linkages that target substrates for degradation (Kristariyanto et al. 2015; Leto et al. 2019; Harris et al. 2021). Trabid is thought to modulate the levels of Lys29/Lys48 mixed chains to regulate proteostasis, autophagy and cell division (Chen et al. 2021; Yu et al. 2021; Vaughan et al. 2022). Lys33-linked ubiquitin polymers have been implicated in post-Golgi protein trafficking (Yuan et al. 2014), and Lys63-linked chains are abundant cellular adducts with established roles in the sorting of endosomal/lysosomal cargo (Erpapazoglou et al. 2014) and mediating the formation of protein assemblies (Tran and Polakis 2012). The second defining feature of Trabid is that it binds the Striatin-interacting phosphatase and kinase (STRIPAK) complex (Sowa et al. 2009; Tran et al. 2013; Harris et al. 2021), a large multiprotein assembly implicated in cytoskeleton organisation, cell migration and neural development (Hwang and Pallas 2014; Sakuma et al. 2014; Madsen et al. 2015; Bazzi et al. 2017; Kuck et al. 2019).

We have previously identified the adenomatous polyposis coli (APC) protein as a candidate Trabid substrate (Tran et al. 2008). Trabid knockdown in HEK293 cells caused APC to become modified with polyubiquitin and aggregate in the cytoplasm, whereas high Trabid levels correlated with *hypo*ubiquitylated APC that accumulated in the membrane protrusions of long cell processes. These observations led us to propose that Trabid regulates the ubiquitylation and subcellular localisation of APC (Tran et al. 2013). In neurons, APC organises the cortical cytoskeleton to promote the formation of growth cones and the steering of growing axons that are essential for embryonic brain development (Yokota et al. 2009; Preitner et al. 2014;

Dogterom and Koenderink 2019; Efimova et al. 2020). High expression of Trabid, APC and STRIPAK proteins in neural stem cells (Castets et al. 2000; Blanpain et al. 2004; Yokota et al. 2009) indicate that Trabid's association with STRIPAK and its ability to regulate APC polyubiquitylation may be important for neurogenesis. We now show that two Trabid mutants found in children with developmental deficits are impaired in two distinct biochemical activities that culminate in the perturbed trafficking of APC to neurite tips. We propose that the neuronal and developmental phenotypes associated with these Trabid loss-of-function mutations are primarily caused by the mislocalisation of APC that leads to defective cytoskeleton organisation and aberrant cell locomotion.

Results

Trabid patient variants are impaired in DUB activity and STRIPAK binding

Trabid/ZRANB1 patient missense mutations, R438W and A451V, are linked to developmental microcephaly (Deciphering Developmental Disorders 2015). Mapping these residues onto the domain structure of Trabid show that they flank either side of Trabid's catalytic cysteine C443 (Fig. 1A). Residue R438 projects prominently into the catalytic cleft formed by the ankyrin repeats and the OTU core of Trabid's catalytic domain (Licchesi et al. 2012), whereas residue A451 resides at the back of the active site, opposite to C443 on alpha helix 4 (Fig. 1B). To determine if patient mutations R438W and A451V influence substrate catalysis, we purified the mutant AnkOTU domains and tested their ability to hydrolyse synthetic ubiquitin chains *in vitro* (Licchesi et al. 2012). Wild-type Trabid AnkOTU generated appreciable amounts of mono-ubiquitin within 15 min incubation with either Lys29- or Lys63-linked di-ubiquitin chains (Fig 1C and D). In contrast, Trabid R438W showed near total loss of DUB activity and cleaved ubiquitin product was only readily detected after a prolonged 120 min incubation (Fig. 1C and D). A catalytically inactive C443S mutant AnkOTU domain failed to hydrolyse ubiquitin chains even after 2 h incubation (Fig. 1C and D). Interestingly, the Trabid A451V AnkOTU domain cleaved Lys29- or Lys63-linked di-ubiquitin with comparable efficiency to wild-type Trabid, despite it being slightly less stable as a recombinant protein based on thermal stability assay (Supplementary Fig. 1A). A ubiquitin suicide probe assay revealed that R438W and A451V

Trabid AnkOTU proteins retained a functional catalytic interaction with ubiquitin (Supplementary Fig. 1B).

In cells, the inability of the DUB-inactive Trabid C443S to cleave polyubiquitin led to stable interaction of this mutant with polyubiquitylated substrates (Tran et al. 2008; Licchesi et al. 2012). We therefore asked whether the DUB-impaired R438W Trabid likewise exhibited increased binding to polyubiquitin in cells. Polyubiquitin chains readily co-precipitated with both FLAG-tagged Trabid R438W and FLAG-Trabid C443S expressed in HEK293T cells, consistent with the compromised DUB activity of these mutants (Fig. 1E). The Trabid A451V variant did not co-precipitate abundant polyubiquitylated substrates, consistent with it retaining full DUB activity (Fig 1E).

We have previously identified an interaction between Trabid and STRIPAK that is important for the deubiquitylation of substrate APC (Tran et al. 2013). Whilst A451V retained full DUB activity, strikingly, in contrast to FLAG-Trabid wild-type, R438W and C443S, the FLAG-Trabid A451V mutant failed to efficiently co-precipitate several STRIPAK components, including Striatin3 and STRIP1 (Fig. 1E). All FLAG-Trabid proteins co-precipitated similar levels of the substrate E3 ubiquitin ligase HECTD1 (Tran et al. 2013; Harris et al. 2021). Together, these results suggest that the Trabid patient mutations produce hypomorphic variants impaired in two distinct biochemical activities: polyubiquitin hydrolysis and STRIPAK-binding.

Decreased cell density in the brains of mice harbouring Trabid patient mutations

Given the microcephaly observed in children with Trabid mutations, and to understand the consequence of Trabid hypomorphic variants *in vivo*, we examined knock-in mice carrying Trabid patient mutations for evidence of brain development abnormalities (Fig. 2A). Mice heterozygous or homozygous for the R438W or A451V mutation were viable, fertile, and born at expected Mendelian ratios (Fig. 2B). Because germline Trabid knockout or C443S homozygous knock-in mice exhibit perinatal lethality (Dickinson et al. 2016) (our unpublished data), these new R438W and A451V mutant mouse strains allow us to interrogate Trabid function *in vivo*. Homozygous mutant mice from the R438W colony weighed on average ~15% less than wild-type littermates, while R438W heterozygous and A451V mutant mice did not exhibit significant

weight loss (Fig. 2C). Immunohistochemical analysis of brain sections from weaned littermate mice of both mutant strains revealed normal structure and laminar organisation of the cerebral cortex, but intriguingly a reduction in cell number was apparent in different brain regions of R438W and A451V homozygous mice compared to wild-type littermate controls (Fig. 2D). The number of Ctip2+ medium spiny neurons in the striatum of R438W and A451V mutant mice were reduced compared with wild-type littermates, and homozygous mice showed a greater cell number loss than heterozygous mice, suggesting a gene dosage effect (Fig. 2E). Moreover, R438W and A451V mutant mice had reduced number of Olig2+ oligodendrocytes in the forebrain and midbrain compared to wild-type littermate mice (Fig. 2F). Olig2+ cells in homozygous brain sections were consistently strongly reduced (>30%) compared to wild-type mice, independent of age or sex. Of a combined 16 sets of littermate mice from both R438W and A451V colonies, reduced neuronal or glial cell numbers were conspicuous in homozygous brain sections of 12 littermate sets (Fig. 2E, F; see also Fig. 3), indicating incomplete penetrance of the mutant phenotype. Collectively, these results suggest that Trabid's DUB and STRIPAK-binding activities are required to produce the correct numbers of neuronal and glial cells in the developing brain.

Trabid mutant mice exhibit a motor deficit consistent with reduced numbers of dopaminergic neurons and projections

Given the cell number deficits in the midbrain of Trabid mutant mice and the reported midbrain neurodegeneration and locomotor defects in Trabid mutant *Drosophila* (Kounatidis et al. 2017), we asked if the numbers of dopaminergic neurons that control motor function might be affected in Trabid R438W and A451V mutant mice. Midbrain and striatal coronal sections were immunostained for Tyrosine Hydroxylase (TH), the rate-limiting enzyme for dopamine synthesis and a marker of dopaminergic neurons. A reduction in the numbers of TH+ neurons was observed in the substantia nigra pars compacta (SNc) of Trabid mutant mice from both R438W and A451V colonies, independent of age or sex (Fig. 3A). SNc neurons project axons to the striatum to produce an extensive network of axonal terminals that communicate with striatal neurons (Matsuda et al. 2009). Consistent with the lack of prominent TH+ neuronal processes emanating from the SNc neurons that remain in the mutant midbrain, TH immunoreactivity was reduced in the striatum of homozygous R438W and A451V mutant mice (Fig. 3B, C). Also in

mutant brain sections, the reduced abundance and intensity of TH+ neuronal processes were readily apparent in cortical regions including the motor cortex and claustrum that regulate motor responses (Fig. 3B, C). Differences in TH staining in the mutant striatum compared to wild-type were modest or not observed in all littermates examined (Fig. 3D), indicating incomplete penetrance of the mutant Trabid alleles.

Given the altered abundance of TH+ cells and projections in motor-related brain regions of Trabid mutant mice, we evaluated the motor function of these mice using a rotarod assay. Homozygous R438W mice showed a significantly reduced latency to fall at 20, 25, 30 and 35 RPM, compared to controls (Fig. 3E), as did homozygous A451V animals at 30 and 35 RPM (Fig. 3E). This indicates that Trabid patient mutations impair motor coordination, consistent with a deficiency in dopaminergic neurons. The smaller size of R438W homozygous mice compared to wild-type littermates (Fig. 2C) could be a contributing factor to the compromised rotarod performance of these mutants. However, given that A451V homozygous mice on average are not smaller than wild-type littermates, the motor deficit exhibited by both R438W and A451V homozygous mice is likely caused by the abnormal cell numbers and reduced dopaminergic neurons in their brains (Figs. 2 and 3). Taken together, these results suggest that Trabid regulates the brain cellular architecture and neuronal circuitry required for normal motor function.

Trabid patient mutants fail to efficiently limit APC ubiquitylation in cells

To understand the molecular basis for the neuronal and behavioral phenotypes of Trabid mutant mice, we focused on APC— an established regulator of mammalian brain development (Yokota et al. 2009; Preitner et al. 2014) and a protein that we have shown becomes strongly ubiquitylated upon loss of Trabid or Striatin (Tran et al. 2008; Tran et al. 2013). Moreover, given that Striatin binds directly to APC (Breitman et al. 2008), we hypothesized that the Trabid patient mutants impaired in DUB activity or Striatin-binding would impact APC ubiquitylation and function in cells. To test this, we generated cells with doxycycline (dox)-inducible expression of FLAG-Trabid and examined the ubiquitylation status of endogenous APC in dox-treated cells. The levels of ubiquitin-modified APC were strongly suppressed in cells expressing wild-type FLAG-Trabid (Fig. 4). In contrast, induction of the FLAG-Trabid R438W mutant, like the catalytically dead FLAG-Trabid C443S, did not repress APC ubiquitylation, and induction of

FLAG-Trabid A451V expression only partially reduced APC ubiquitylation compared to control cells (Fig. 4). These results suggest that both DUB and STRIPAK-binding activities of Trabid are required for efficient deubiquitylation of APC in cells.

Trabid patient mutants impede EGFP-APC transport to the leading edge of migrating cells

APC decorates the membrane protrusions at the leading edge of migrating cells (Nathke et al. 1996) and we have shown that Trabid is a key regulator of APC localisation to these cortical structures (Tran et al. 2013). Consistent with this insight, FLAG-Trabid localised prominently with EGFP-APC in the tips of long cell processes (Fig. 5A). Analysis of several of these tip clusters by super resolution microscopy revealed ~30% overlap between the FLAG-Trabid and EGFP-APC signals, indicating that a significant fraction of these proteins co-localise in cortical cell protrusions (Fig. 5B). In sub-confluent cultures, EGFP-APC localised strongly to the lamellipodial leading edge of the majority of cells co-transfected wild-type FLAG-Trabid (Fig. 5C, D). By contrast, in cells transfected with the FLAG-Trabid mutants R438W and A451V, EGFP-APC formed irregular puncta at sub-cortical regions close to the leading edge and EGFP-APC aggregates are often sequestered to puncta formed by the R438W FLAG-Trabid mutant (Fig. 5C, D). Such sites may contain ubiquitylated substrates bound to DUB-defective Trabid mutants, as we have previously demonstrated with Trabid C443S (Tran et al. 2008; Licchesi et al. 2012). Consistently, FLAG-Trabid C443S formed puncta that contained EGFP-APC near the tips of long cell processes (Fig. 5E). The Trabid substrate HECTD1 was sequestered to C443S puncta in the cytosol, but intriguingly not to puncta residing in proximity of the leading edge membrane (Fig. 5E). In near-confluent cultures following prolonged co-transfection of FLAG-Trabid mutants and EGFP-APC, we observed the striking phenomena of strong EGFP-APC aggregation on or near the plasma membrane and thin tube-like processes extending between neighbouring cells decorated with abundant EGFP-APC puncta/aggregates of various sizes (Fig. 5F). In cells co-transfected with wild-type FLAG-Trabid, EGFP-APC concentrated in cell tips (Fig. 5F). Collectively, these results indicate that Trabid's DUB and STRIPAK-binding activities are required for the efficient localisation of APC to plasma membrane sites involved in polarised cell migration.

Trabid patient mutations perturb the axonal trafficking of APC-tdTomato and impair the trajectory of neurite outgrowth

APC regulates the dynamic interactions of the microtubule and actin cytoskeletons at cortical membranes to direct the formation of neuronal growth cones and the trajectory of axon growth (Dogterom and Koenderink 2019). To investigate the effect of patient Trabid mutations on APC localisation in primary neurons, we generated mice expressing an APC-tdTomato fluorescent protein under the control of the endogenous *Apc* gene promoter (Fig. 6A). APC-tdTomato mice were bred with knock-in mice carrying either the Trabid R438W or A451V mutant allele (Fig. 2) and neural progenitors were isolated at embryonic day E11.5 from compound heterozygotes. We then performed live cell imaging to analyse the trafficking of APC-tdTomato in neurites extending from progenitors undergoing differentiation (Fig. 6A). Endogenous Trabid protein levels were comparable in neural progenitor cultures derived from embryos bearing wild-type or R438W and A451V mutant Trabid alleles (Fig. 6B). In neurons with wild-type Trabid, APC-tdTomato accumulated strongly in the tips of growing neurites, marking prominent growth cones that drive axon elongation (Fig. 6C; *Zranb1*$^{+/+}$). In neurons with heterozygous Trabid R438W or A451V mutation, APC-tdTomato exhibited broad distribution along the length of the neurite and the formation of growth cones were severely compromised (Fig. 6C, *Zranb1*$^{R438W/+}$). Tracking analysis of the turn angles of APC-tdTomato intensities revealed that neurites with wild-type Trabid elongated in a polarised manner, whereas neurites with R438W or A451V mutant Trabid turned back or retracted at a greater frequency (Fig. 6D and E). These data suggest that Trabid's DUB and STRIPAK-binding activities are required for efficient transport of APC to neurite tips to promote the formation growth cones required for polarised axon elongation.

Discussion

We describe a novel function for the deubiquitylating enzyme Trabid as a key regulator of axonal growth and guidance that likely underpins the neurodevelopmental defects observed in children with Trabid mutation. Our data suggests that Trabid's mechanism of action is to suppress the ubiquitylation of APC to regulate its intracellular trafficking. A *hypo*ubiquitylated APC pool is efficiently localised to the cortical cytoskeleton where it directs neuronal growth cone formation and polarised axon elongation. The identification of human Trabid variants that

disrupt the distribution of APC to the leading edge of migrating cells provides a plausible explanation for the associated patient neuro-developmental disorders. Our work identifies Trabid's DUB- and STRIPAK-binding activities, and the control of APC localisation, as crucial events during embryonic and neural development.

The two patients carrying Trabid missense mutations R438W and A451V were diagnosed with a range of distinct congenital disorders including craniofacial abnormalities, seizures, developmental delay, autism—and both patients presented with microcephaly and constipation (Deciphering Developmental Disorders 2015). We propose that the underlying cause of these seemingly unrelated conditions, broadly classified as neurocristopathies, is the abnormal specification or migration of neural crest cells in the developing embryo (Vega-Lopez et al. 2018). Discrete neural crest populations contribute to the development of craniofacial structures, the forebrain and midbrain, and the enteric nervous system (Anderson et al. 2006; Creuzet et al. 2006). Therefore, errors in the formation or polarised migration of neural crest cells could account for all the patient phenotypes, including the reduction in brain volume (microcephaly). Presently, we can only speculate that the irregular cellular architecture and reduced cell numbers in the brains of mice harbouring Trabid patient mutations (Figs. 2 and 3) reflect the errant migration of neural crest or neural progenitor cell populations in early embryogenesis (Silva et al. 2019). While Trabid mutant mice did not exhibit microcephaly, they showed a motor deficit (Fig. 3) consistent with the locomotor defects reported for Trabid loss-of-function in *Drosophila* (Kounatidis et al. 2017). Intriguingly, the fly Striatin homolog CKA is involved in axonal transport and motor coordination (Neisch et al. 2017), and *Drosophila* Strip1 regulates endosomal trafficking and axon elongation (Sakuma et al. 2014). Endosomal trafficking defects have been linked to reduced proliferation of neural progenitors and microcephaly (Carpentieri et al. 2022). Three independent groups have identified Trabid's association with STRIPAK (Sowa et al. 2009; Tran et al. 2013; Harris et al. 2021). We have now established the functional significance of this interaction. The requirement of Trabid binding to STRIPAK for efficient protein trafficking, polarised axon growth, and motor coordination (Figs. 3, 5, 6), supports the view that Trabid-STRIPAK regulates an evolutionarily conserved mechanism of cell movement required for normal brain development and establishment of the correct neuronal circuitry in the motor system.

The impairment of two distinct Trabid functions—polyubiquitin hydrolysis and STRIPAK-binding—led to common cellular, developmental, and behavioral phenotypes (Figs. 2-6) (Deciphering Developmental Disorders 2015), strongly suggesting that these activities act in the same pathway. We propose that APC is the primary molecular target of Trabid action in cytoskeleton organisation and polarised axon growth (Fig. 7). APC is an established regulator of cell adhesion and migration, and it governs the cortical actin and microtubule cytoskeleton dynamics required to form and steer axonal growth cones (Dogterom and Koenderink 2019; Efimova et al. 2020). In a yeast two hybrid screen, we have found that Trabid and Striatin interacted with the armadillo repeat domain (ARD) of APC, but not to an APC ARD mutant that caused cell-cell adhesion defects (Hamada and Bienz 2002; Tran et al. 2008). This implies that a functional interaction between Trabid, Striatin and APC promotes the fidelity of cell-cell or cell-substratum contacts. Our model of Trabid action in Figure 7 integrates published data showing that (1) Trabid complexes with Striatin/STRIPAK in human cell lines (Sowa et al. 2009; Tran et al. 2013; Harris et al. 2021), and (2) Striatin binds directly to the ARD domain of APC (Breitman et al. 2008). We propose that STRIPAK recruits Trabid to deubiquitylate APC. This allows APC to accumulate at the leading edge of migrating cells to promote efficient, polarised locomotion (Fig. 7A). The Trabid R438W mutant still binds STRIPAK and is recruited to APC, but it is impaired in its ability to cleave ubiquitin chains from APC. And although the Trabid A451V mutant retains full DUB activity, it cannot be recruited to APC via STRIPAK. Both mutant scenarios cause APC to become persistently modified with ubiquitin chains that lead to APC delocalisation from cell tips and defective cell movement (Fig. 7B). Consistent with this model, Trabid and/or Striatin deficiency caused APC hyperubiquitylation and aggregation, perturbed actin assembly and microtubule stability, and inhibited the migration of mouse and human cell lines (Bai et al. 2011; Tran et al. 2013) (our unpublished data).

We have shown that ubiquitin-modified APC correlated with its binding to Axin in the β-catenin destruction complex (Tran and Polakis 2012), whereas non-ubiquitin-modified APC accumulates in membrane protrusions (Tran et al. 2013). Thus, reversible modification with polyubiquitin could be the long-hypothesised molecular switch that regulates the distribution of APC between its many functional pools in cells (Dikovskaya et al. 2001; Bienz 2002). Chronic APC

ubiquitylation in Trabid deficient/mutant cells might result in increased APC sequestration into Axin destruction complexes or promote spurious interactions with ubiquitin binding proteins that retard APC trafficking along microtubules. Rescue of the APC transport defect could hypothetically be achieved by inhibition of glycogen synthase kinase 3 (GSK3), which we have shown abolishes APC ubiquitylation (Tran and Polakis 2012). In support of this idea is the finding that GSK3 inactivation promotes the association of APC with microtubule plus ends to drive polarised cell migration (Etienne-Manneville and Hall 2003).

Optimal cell migration and adhesion requires stable, acetylated microtubules (Aguilar et al. 2014; Bance et al. 2019). Of note, loss of APC and the STRIPAK proteins STRIP1 and CTTNBP2 strongly reduced the acetylated microtubule network in neurons (Yokota et al. 2009; Shih et al. 2014; Sakuma et al. 2015). Furthermore, Striatin depletion perturbed cell-cell adhesion (Breitman et al. 2008; Lahav-Ariel et al. 2019) and axon elongation defects caused by STRIP1 mutation are linked to the dysregulation of neuronal adhesion (Sakuma et al. 2014). It would be interesting to investigate if chronic APC ubiquitylation and dysfunction underlie all Trabid and STRIPAK mutant phenotypes.

Materials and Methods

Protein purification and characterisation

Wild-type (WT), R438W, A451V, and C443S Trabid AnkOTU domains (245-697) were expressed in BL21 competent *E. coli* and purified as described previously (Licchesi et al. 2012) with minor modifications. *E. coli* cells were induced with 300 mM IPTG and grown overnight at 16°C. Cells were lysed by sonication in 50 mL lysis buffer (20 mM Tris pH 8.5, 200 mM NaCl, 10% glycerol, 1 mM PMSF, 2x Roche protease inhibitor tablets, 3 mM $MgCl_2$, 0.1 mg/mL DNAse, 150 µL lysozyme, 10 mM β-mercaptoethanol) per 2 L culture. Anion-exchange chromatography (MonoQ 5/50) was performed using the ÄKTA pure system at 4°C. See Supplementary Figure 1 for the characterisation of the thermal stability and ubiquitin reactivity of purified Trabid AnkOTU proteins. For DUB assays, a total of 20 µL reaction consisting of 0.25 µM purified AnkOTU domain was incubated with 1 µM of K29, K63 di-ubiquitin chains, or K33-linked Tetra-Ub chains (R&D Systems) in DUB reaction buffer (50 mM NaCl, 50 mM Tris

pH 7.4, and 5 mM DTT) at 37°C. Reactions were stopped at the indicated times by addition of SDS sample buffer and visualized by SDS-PAGE and silver staining (Silver Stain Plus; Biorad).

Cells, plasmids, and antibodies

An inducible lentiviral CRISPR/Cas9 system (Aubrey et al. 2015) was used to overexpress Trabid in Figure 4. PCR amplified DNA encoding human wild-type or mutant Trabid with an N-terminal FLAG tag was cloned into the EcoRI/NheI sites of a doxycycline-inducible pFTREtight MCS rtTAadvanced puro lentiviral vector (Brumatti et al. 2013). Transduced HEK293 cells were selected for puromycin resistance and pooled clones were used for experiments. Transient transfection of plasmids pcDNA3.1-FLAG-Trabid (Tran et al. 2013), FLAG-Trabid mutants generated by site-directed mutagenesis (QuikChange, Agilent), pEGFP-C1-APC (Rosin-Arbesfeld et al. 2001), and pCMV-HA-HECTD1 (Sarkar and Zohn 2012) in HEK293T cells was performed using Lipofectamine 2000 (Invitrogen). HEK293T cells (ATCC) and HEK293 cells (Cellbank Australia) were authenticated by STR profiling and frequently tested for mycoplasma contamination. Cells were cultured in DMEM supplemented with 10% FBS and 2 mM L-Glutamine in a humidified incubator at 37°C with 5% CO_2. Mouse monoclonal Trabid antibodies and rabbit polyclonal HectD1 antibodies have been described (Tran et al. 2013). Commercial antibodies were purchased from a variety of vendors: anti-APC ALi 12-28 (Santa Cruz), anti-Striatin (BD Biosciences), anti-Striatin3 (SG2NA, Novus Biologicals), anti-Strip1 (Abcepta) anti-ubiquitin P4D1 (Cell Signaling), anti-FLAG M2, anti-β-actin-HRP AC-15, anti-β-tubulin (Sigma), anti-HA 3F10 (Roche), anti-Tyrosine Hydroxylase (Millipore, AB152), anti-Ctip2 (Abcam, ab18465), and anti-Olig2 (Abcam, ab109186).

Protein enrichment from cell lysates

Confluent cells in 10 cm dishes were lysed on ice in 1 mL lysis buffer containing 1% IGEPAL CA-630, 50 mM Tris-HCl, pH 7.5, 120 mM NaCl, 1 mM EDTA, and protease inhibitor tablets (Roche). Lysates were centrifuged at 14,000 rpm for 10 min to remove cell debris. The supernatant was assayed for protein (BCA kit, Pierce), then 1 mg total protein was immunoprecipitated with anti-FLAG M2 antibody and protein G sepharose in a total volume of 1 mL lysis buffer. Enrichment of polyubiquitin chains was performed using purified GST-TUBE (Tandem Ubiquitin Binding Entity) protein (Hjerpe et al. 2009). A volume of cell supernatant

containing 1 mg total protein was diluted 1:1 with 4M urea then incubated with 10 µg GST-TUBE and Glutathione sepharose 4B. Immunoprecipitations and GST-TUBE pulldowns were performed overnight with constant rotation at 4°C. Protein complexes were washed twice with lysis buffer and once with PBS, then eluted at 95°C for 5 min in Laemmli buffer for Western blotting analysis.

Mice

All mouse studies complied with relevant ethical regulations and were approved by the Walter and Eliza Hall Institute Animal Ethics Committee. The *Zranb1*^{R438W}, *Zranb1*^{A451V}, and *Apc*^{tdTomato} knock-in mice were generated on a C57BL/6J background using CRISPR–Cas9-mediated gene editing by the Melbourne Advanced Genome Editing Centre (MAGEC) at the Walter and Eliza Hall Institute. To generate a R438W mutation within the *Zranb1* gene on mouse chromosome 7, a single guide (sg) RNA of the sequence GAC TAT ATG CAC TTT GGA AC was used to create double stranded breaks within the Zranb1 locus to stimulate homologous recombination and an oligo donor of the sequence TAT AAA CTG GTC TTT GGA GTT GGC TAC ACG TCT GGA CAG TAG ACT ATA TGC ACT TTG GAA CTG GAC TGC CGG AGA TTG TTT ACT TGA CTC AGT ACT ACA AGC TAC ATG GGG CAT TTA TGA CAA A was used to introduce the R438W mutation. The sgRNA and donor sequence along with Cas9 mRNA were injected into the cytoplasm of fertilized one-cell stage embryos generated from wild-type C57BL/6J breeders. To generate the A451V mutation, a sgRNA of the sequence ACT CAG TAC TAC AAG CTA CA and an oligo donor of the sequence ACA GTA GAC TAT ATG CAC TTT GGA ACC GGA CTG CCG GAG ATT GTT TAC TTG ACT CAG TAC TAC AAG TCA CAT GGG GCA TTT ATG ACA AAG ACT CGG TGC TTC GGA AAG CCC TGC ATG ACA GCC TG CAT was used. Twenty-four hours later, two-cell stage embryos were transferred into the uteri of pseudo-pregnant female mice. Viable offspring were genotyped by next-generation sequencing. Targeted animals were backcrossed twice to wild-type C57BL/6J to eliminate off-target mutations. Generation of C57BL/6J mice expressing the APC-tdTomato fusion protein under the control of the endogenous *Apc* promoter (B6J.*Apc*^{tdTom}) were based on methods previously described (Ng et al. 2020). Briefly, a sgRNA of the sequence AGA CGT CAC GAG GTA AGA CC was used to create double stranded breaks within the *Apc* locus to stimulate homologous recombination. A targeting vector containing homology arms of ~1.4 kilobases was

used to introduce the tdTomato coding sequence after the last *Apc* coding exon. Forward (ACC TGT TCC TGT ACG GCA TG) and reverse (GCC TCC CAA AAT GAC CAG TG) primers to detect the tdTomato sequence were used to screen viable pups for integration of the targeting vector by PCR.

Neurite outgrowth from cultured neural progenitors

To generate mouse embryos expressing Apc-tdTomato with wild-type or mutant Trabid, mice heterozygous for the Apc-tdTomato allele ($Apc^{tdTom/+}$) were outcrossed with mice heterozygous for the Trabid R438W or A451V mutant allele ($Zranb1^{R438W/+}$ or $Zranb1^{A451V/+}$). Embryos at E11.5 were harvested from pregnant females and ventral midbrains were dissected as previously described (Thompson and Parish 2013). The isolated midbrain tissue was enzymatically dissociated in Hank's Balanced Salt Solution containing 0.05% trypsin and 0.1% DNase I for 12 minutes at 37°C. Cells in the tissue were separated by mechanical dissociation, counted, then plated in serum-free N2 medium consisting of a 1:1 mixture of Ham's F12 and Minimum Essential Medium supplemented with 15 mM HEPES buffer, 1 mM glutamine, 6 mg/ml glucose, 1 mg/ml bovine serum albumin and N2 100X supplement. Cells were seeded at a density of 250,000 cells per well in a 24-well plate at 37°C, 3% CO_2. An aliquot of the resultant neurosphere cultures were sequenced to ascertain genotypes. To differentiate midbrain progenitors towards the dopaminergic lineage, neurospheres were resuspended in N2 medium containing BDNF and GDNF (30 ng/ml each) then seeded in glass bottom ibidi chamber slides pre-coated with poly-D-lysine and laminin (10 µg/ml each) for live imaging of neurite outgrowth as described below.

Histology and IHC analysis

Mice were euthanized by CO_2 inhalation and intracardial perfusion was performed to fix the tissues. Perfusion was initiated with Dulbecco's phosphate buffered saline followed by 10% neutral buffered formalin (NBF). After perfusion, brain and tissues were dissected and post-fixed in 10% NBF for 24h before paraffin-embedding with the Tissue-Tek VIP 6 automated tissue processor (Sakura Finetek USA). Formalin-fixed paraffin-embedded tissues were sectioned into 7 µm slices using a microtome and mounted on positively charged slides. Immunohistochemistry (IHC) was performed with the Omnis Auto-immunostaining platform

using Agilent EnVision Target retrieval solution and the optimal dilution of the primary antibody against the target protein. Secondary antibody detection was performed with the Dako EnVision+ Single Reagents HRP and FLEX DAB+ Substrate Chromogen System. Slides were counterstained with haematoxylin. Sections from wild-type, heterozygous and homozygous littermate mice were mounted and stained on the same slide to ensure IHC signals can be directly compared. Cell counts and IHC signal intensities were quantified using Fiji software (NIH). The workflow for counting cells from IHC images is described in Supplementary Figure 2. IHC signal intensities were measured as the optical density proportional to the concentration of the stain. Briefly, the colour spectra of DAB- and haematoxylin-stained image was separated by colour deconvolution, converted to greyscale, thresholding was applied, and the mean pixel intensity of the region of interest was measured.

Rotarod performance test

The motor coordination of 3- to 4-month-old littermate mice from Trabid R438W and A451V colonies were measured using a rotating rod (Rotamex-5, Columbus Instruments). Mice were lowered onto a 3 cm diameter rod rotating at 12, 16, 20, 25, 30, 35, 40 or 45 revolutions per min (RPM) for 2 min or until they fell. Animals were given a 5 min rest between RPM sessions. Two trials were performed with a 1 h break between trials. The latency to fall was recorded for each RPM. A 1 sec penalty was added if an animal failed to walk in time with the rod but rather gripped the rod and rotated with it (cartwheel). Animals underwent 2 trials per day across 3 days.

Microscopy and image analysis

Confocal microscopy – Cells grown in Lab-Tek II chamber slides were fixed with 4% paraformaldehyde for 10 min at room temperature, then permeabilized with 0.2% Triton-X100 and blocked with 5% normal goat serum (NGS). Cells were incubated with primary antibodies diluted in 5% NGS overnight at 4ºC, followed by Alexa Fluor-conjugated secondary antibodies for 1h at room temperature. ProLong Gold antifade reagent with DAPI was used to mount coverslips to microscope slides. Confocal images were acquired on a Zeiss LSM 880 Airyscan microscope using a 63x/1.4 N.A. oil objective, and 405, 488 and 594nm lasers. Maximum intensity projections of raw images comprising 10-15 *z* sections were created using Fiji.

3D structured illumination microscopy – Super-resolution three-dimensional structured illumination microscopy (3D-SIM) was performed on the DeltaVision OMX-SR system using a 60x/1.42 N.A. PlanApo oil immersion objective, sCMOS cameras, and 488, 568 and 640 nm lasers. 3D-SIM images consisted of 15 raw images per focal plane per colour channel with 125 nm between each z-step. Images were reconstructed and the colour channels aligned using the reconstruction and alignment algorithms in softWoRx 7.0. Fraction of overlap between FLAG-Trabid and EGFP-APC were measured in Imaris 9.2.

Lattice lightsheet time-lapse imaging and analysis – Live cell time-lapse imaging of APC-tdTomato fluorescence in growing neurites was acquired using the Zeiss Lattice Light Sheet 7 microscope. A 561 nm laser formed a light sheet of length 30 µm with a thickness of 1 µm at the sample plane via a 13.3 x, 0.44 NA objective. tdTomato fluorescence was collected via a 44.83 X, 1 NA detection objective lens. Data was collected with a frame rate of 60 ms and a z-step of 300 nm. Each region was imaged at 15-min intervals for 4-6 hours. Fluorescence was collected via a multi-band stop, LBF 405/488/561/633, filter. Images were subsequently deskewed using Zeiss's Zen 3.4 software. Samples were measured at 37°C and 5% CO_2. Maximum intensity projections were created from the deskewed data in Fiji. Neurite tips were tracked using Trackmate (v6.0.3) and LoG detector with 12 µm diameter, 0.08 threshold, no filters, and subpixel localisation turned on. A minimum of 5 frames were set for track inclusion. Turn angles were calculated using Matlab R2019b. Three points were used to calculate the turn. The first two points determine the direction of neurite growth. The angle between this direction to the third point determines the turn angle of the neurite. The turn angle was normalized such that 0º constitutes a step straight forward with no turn and 180º is a turn backwards.

Acknowledgements

We are indebted to Prof David L. Vaux for his generous support and mentorship in the early stages of this study. We thank Drs S. Wilcox, S. Scutts, J. Heath, D. Newgreen, J. Vince, C. Parish, K. Scicluna, M. Herold, V. Wimmer, T. Thomas, K. Newton and V. Dixit for discussion, reagents and technical support; and WEHI's Bioservices staff for outstanding animal care. Part of the funding for this study was provided by the Australian National Health and Medical

Research Council (Ideas Grant #1181580 to E.V., H.T., and B.M.T). G.D. was supported by a fellowship from the Bodhi Education Fund. Work in the authors' laboratory is made possible by operational infrastructure grants through the Australian Government Independent Research Institutes Infrastructure Support (IRISS) and the Victorian State Government OIS. The generation of all mutant and transgenic mice used in this study was supported by Phenomics Australia and the Australian Government through the National Collaborative Research Infrastructure Strategy (NCRIS) program.

Author Contributions

D.F. designed and performed the protein biochemistry experiments, quantified cell numbers from histological sections, and assisted with the generation and maintenance of neurosphere cultures. M.B. designed and performed the rotarod experiments and assisted with analysis of the rotarod and histology data. M.M. performed 3D-SIM microscopy, live cell imaging of Apc-tdTomato trafficking, and analysed the data. A.K. designed the targeting vectors for generation of knock-in mice. E.T. assisted with the design of histology experiments. C.H. performed the genotyping. G.K. assisted with statistical analysis of the rotarod data and quantified IHC intensities. A.V., C.M., M.F., K.R., B.T., and E.V. analysed data. D.K. analysed data and provided study feedback and advice. G.D. supervised the study, analysed and conceptualized data, and edited the manuscript. H.T. conceived the project, designed, performed and supervised experiments, analysed and conceptualized data, and wrote the manuscript. All authors have read and commented on the manuscript.

Competing Interest Statement

D.K. is founder, shareholder and serves on the SAB of Entact Bio.

References

Aguilar A, Becker L, Tedeschi T, Heller S, Iomini C, Nachury MV. 2014. Alpha-tubulin K40 acetylation is required for contact inhibition of proliferation and cell-substrate adhesion. *Mol Biol Cell* **25**: 1854-1866.

Anderson RB, Newgreen DF, Young HM. 2006. Neural crest and the development of the enteric nervous system. *Adv Exp Med Biol* **589**: 181-196.

Aubrey BJ, Kelly GL, Kueh AJ, Brennan MS, O'Connor L, Milla L, Wilcox S, Tai L, Strasser A, Herold MJ. 2015. An inducible lentiviral guide RNA platform enables the identification of tumor-essential genes and tumor-promoting mutations in vivo. *Cell Rep* **10**: 1422-1432.

Bai SW, Herrera-Abreu MT, Rohn JL, Racine V, Tajadura V, Suryavanshi N, Bechtel S, Wiemann S, Baum B, Ridley AJ. 2011. Identification and characterization of a set of conserved and new regulators of cytoskeletal organization, cell morphology and migration. *BMC Biol* **9**: 54.

Bance B, Seetharaman S, Leduc C, Boeda B, Etienne-Manneville S. 2019. Microtubule acetylation but not detyrosination promotes focal adhesion dynamics and astrocyte migration. *J Cell Sci* **132**.

Bazzi H, Soroka E, Alcorn HL, Anderson KV. 2017. STRIP1, a core component of STRIPAK complexes, is essential for normal mesoderm migration in the mouse embryo. *Proc Natl Acad Sci U S A* **114**: E10928-E10936.

Beck DB, Basar MA, Asmar AJ, Thompson JJ, Oda H, Uehara DT, Saida K, Pajusalu S, Talvik I, D'Souza P et al. 2021. Linkage-specific deubiquitylation by OTUD5 defines an embryonic pathway intolerant to genomic variation. *Sci Adv* **7**.

Bienz M. 2002. The subcellular destinations of APC proteins. *Nat Rev Mol Cell Biol* **3**: 328-338.

Blanpain C, Lowry WE, Geoghegan A, Polak L, Fuchs E. 2004. Self-renewal, multipotency, and the existence of two cell populations within an epithelial stem cell niche. *Cell* **118**: 635-648.

Breitman M, Zilberberg A, Caspi M, Rosin-Arbesfeld R. 2008. The armadillo repeat domain of the APC tumor suppressor protein interacts with Striatin family members. *Biochim Biophys Acta* **1783**: 1792-1802.

Brumatti G, Salmanidis M, Kok CH, Bilardi RA, Sandow JJ, Silke N, Mason K, Visser J, Jabbour AM, Glaser SP et al. 2013. HoxA9 regulated Bcl-2 expression mediates survival of

myeloid progenitors and the severity of HoxA9-dependent leukemia. *Oncotarget* **4**: 1933-1947.

Carpentieri JA, Di Cicco A, Lampic M, Andreau D, Del Maestro L, El Marjou F, Coquand L, Bahi-Buisson N, Brault JB, Baffet AD. 2022. Endosomal trafficking defects alter neural progenitor proliferation and cause microcephaly. *Nat Commun* **13**: 16.

Castets F, Rakitina T, Gaillard S, Moqrich A, Mattei MG, Monneron A. 2000. Zinedin, SG2NA, and striatin are calmodulin-binding, WD repeat proteins principally expressed in the brain. *J Biol Chem* **275**: 19970-19977.

Chen YH, Huang TY, Lin YT, Lin SY, Li WH, Hsiao HJ, Yan RL, Tang HW, Shen ZQ, Chen GC et al. 2021. VPS34 K29/K48 branched ubiquitination governed by UBE3C and TRABID regulates autophagy, proteostasis and liver metabolism. *Nat Commun* **12**: 1322.

Clague MJ, Urbe S, Komander D. 2019. Breaking the chains: deubiquitylating enzyme specificity begets function. *Nat Rev Mol Cell Biol*.

Creuzet SE, Martinez S, Le Douarin NM. 2006. The cephalic neural crest exerts a critical effect on forebrain and midbrain development. *Proc Natl Acad Sci U S A* **103**: 14033-14038.

Deciphering Developmental Disorders S. 2015. Large-scale discovery of novel genetic causes of developmental disorders. *Nature* **519**: 223-228.

Dickinson ME, Flenniken AM, Ji X, Teboul L, Wong MD, White JK, Meehan TF, Weninger WJ, Westerberg H, Adissu H et al. 2016. High-throughput discovery of novel developmental phenotypes. *Nature* **537**: 508-514.

Dikovskaya D, Zumbrunn J, Penman GA, Nathke IS. 2001. The adenomatous polyposis coli protein: in the limelight out at the edge. *Trends Cell Biol* **11**: 378-384.

Dogterom M, Koenderink GH. 2019. Actin-microtubule crosstalk in cell biology. *Nat Rev Mol Cell Biol* **20**: 38-54.

Efimova N, Yang C, Chia JX, Li N, Lengner CJ, Neufeld KL, Svitkina TM. 2020. Branched actin networks are assembled on microtubules by adenomatous polyposis coli for targeted membrane protrusion. *J Cell Biol* **219**.

Erpapazoglou Z, Walker O, Haguenauer-Tsapis R. 2014. Versatile roles of k63-linked ubiquitin chains in trafficking. *Cells* **3**: 1027-1088.

Etienne-Manneville S, Hall A. 2003. Cdc42 regulates GSK-3beta and adenomatous polyposis coli to control cell polarity. *Nature* **421**: 753-756.

618 Hamada F, Bienz M. 2002. A Drosophila APC tumour suppressor homologue functions in cellular
619 adhesion. *Nat Cell Biol* **4**: 208-213.
620 Harris LD, Le Pen J, Scholz N, Mieszczanek J, Vaughan N, Davis S, Berridge G, Kessler BM,
621 Bienz M, Licchesi JDF. 2021. The deubiquitinase TRABID stabilizes the K29/K48-
622 specific E3 ubiquitin ligase HECTD1. *J Biol Chem* **296**: 100246.
623 Hjerpe R, Aillet F, Lopitz-Otsoa F, Lang V, England P, Rodriguez MS. 2009. Efficient protection
624 and isolation of ubiquitylated proteins using tandem ubiquitin-binding entities. *EMBO Rep*
625 **10**: 1250-1258.
626 Hwang J, Pallas DC. 2014. STRIPAK complexes: structure, biological function, and involvement
627 in human diseases. *Int J Biochem Cell Biol* **47**: 118-148.
628 Komander D, Clague MJ, Urbe S. 2009. Breaking the chains: structure and function of the
629 deubiquitinases. *Nat Rev Mol Cell Biol* **10**: 550-563.
630 Kounatidis I, Chtarbanova S, Cao Y, Hayne M, Jayanth D, Ganetzky B, Ligoxygakis P. 2017. NF-
631 kappaB Immunity in the Brain Determines Fly Lifespan in Healthy Aging and Age-Related
632 Neurodegeneration. *Cell Rep* **19**: 836-848.
633 Kristariyanto YA, Abdul Rehman SA, Campbell DG, Morrice NA, Johnson C, Toth R, Kulathu
634 Y. 2015. K29-selective ubiquitin binding domain reveals structural basis of specificity and
635 heterotypic nature of k29 polyubiquitin. *Mol Cell* **58**: 83-94.
636 Kuck U, Radchenko D, Teichert I. 2019. STRIPAK, a highly conserved signaling complex,
637 controls multiple eukaryotic cellular and developmental processes and is linked with
638 human diseases. *Biol Chem* **400**: 1005-1022.
639 Lahav-Ariel L, Caspi M, Nadar-Ponniah PT, Zelikson N, Hofmann I, Hanson KK, Franke WW,
640 Sklan EH, Avraham KB, Rosin-Arbesfeld R. 2019. Striatin is a novel modulator of cell
641 adhesion. *FASEB J* **33**: 4729-4740.
642 Leto DE, Morgens DW, Zhang L, Walczak CP, Elias JE, Bassik MC, Kopito RR. 2019. Genome-
643 wide CRISPR Analysis Identifies Substrate-Specific Conjugation Modules in ER-
644 Associated Degradation. *Mol Cell* **73**: 377-389 e311.
645 Licchesi JD, Mieszczanek J, Mevissen TE, Rutherford TJ, Akutsu M, Virdee S, El Oualid F, Chin
646 JW, Ovaa H, Bienz M et al. 2012. An ankyrin-repeat ubiquitin-binding domain determines
647 TRABID's specificity for atypical ubiquitin chains. *Nature structural & molecular biology*
648 **19**: 62-71.

649 Madsen CD, Hooper S, Tozluoglu M, Bruckbauer A, Fletcher G, Erler JT, Bates PA, Thompson
650 B, Sahai E. 2015. STRIPAK components determine mode of cancer cell migration and
651 metastasis. *Nat Cell Biol* **17**: 68-80.
652 Matsuda W, Furuta T, Nakamura KC, Hioki H, Fujiyama F, Arai R, Kaneko T. 2009. Single
653 nigrostriatal dopaminergic neurons form widely spread and highly dense axonal
654 arborizations in the neostriatum. *J Neurosci* **29**: 444-453.
655 Nathke IS, Adams CL, Polakis P, Sellin JH, Nelson WJ. 1996. The adenomatous polyposis coli
656 tumor suppressor protein localizes to plasma membrane sites involved in active cell
657 migration. *J Cell Biol* **134**: 165-179.
658 Neisch AL, Neufeld TP, Hays TS. 2017. A STRIPAK complex mediates axonal transport of
659 autophagosomes and dense core vesicles through PP2A regulation. *J Cell Biol* **216**: 441-
660 461.
661 Ng SS, De Labastida Rivera F, Yan J, Corvino D, Das I, Zhang P, Kuns R, Chauhan SB, Hou J,
662 Li XY et al. 2020. The NK cell granule protein NKG7 regulates cytotoxic granule
663 exocytosis and inflammation. *Nat Immunol* **21**: 1205-1218.
664 Preitner N, Quan J, Nowakowski DW, Hancock ML, Shi J, Tcherkezian J, Young-Pearse TL,
665 Flanagan JG. 2014. APC is an RNA-binding protein, and its interactome provides a link to
666 neural development and microtubule assembly. *Cell* **158**: 368-382.
667 Rosin-Arbesfeld R, Ihrke G, Bienz M. 2001. Actin-dependent membrane association of the APC
668 tumour suppressor in polarized mammalian epithelial cells. *EMBO J* **20**: 5929-5939.
669 Sakuma C, Kawauchi T, Haraguchi S, Shikanai M, Yamaguchi Y, Gelfand VI, Luo L, Miura M,
670 Chihara T. 2014. Drosophila Strip serves as a platform for early endosome organization
671 during axon elongation. *Nat Commun* **5**: 5180.
672 Sakuma C, Okumura M, Umehara T, Miura M, Chihara T. 2015. A STRIPAK component Strip
673 regulates neuronal morphogenesis by affecting microtubule stability. *Sci Rep* **5**: 17769.
674 Sarkar AA, Zohn IE. 2012. Hectd1 regulates intracellular localization and secretion of Hsp90 to
675 control cellular behavior of the cranial mesenchyme. *J Cell Biol* **196**: 789-800.
676 Shih PY, Lee SP, Chen YK, Hsueh YP. 2014. Cortactin-binding protein 2 increases microtubule
677 stability and regulates dendritic arborization. *J Cell Sci* **127**: 3521-3534.
678 Silva CG, Peyre E, Nguyen L. 2019. Cell migration promotes dynamic cellular interactions to
679 control cerebral cortex morphogenesis. *Nat Rev Neurosci* **20**: 318-329.

Sowa ME, Bennett EJ, Gygi SP, Harper JW. 2009. Defining the human deubiquitinating enzyme interaction landscape. *Cell* **138**: 389-403.

Thompson LH, Parish CL. 2013. Transplantation of fetal midbrain dopamine progenitors into a rodent model of Parkinson's disease. *Methods Mol Biol* **1059**: 169-180.

Tran H, Bustos D, Yeh R, Rubinfeld B, Lam C, Shriver S, Zilberleyb I, Lee MW, Phu L, Sarkar AA et al. 2013. HectD1 E3 ligase modifies adenomatous polyposis coli (APC) with polyubiquitin to promote the APC-axin interaction. *J Biol Chem* **288**: 3753-3767.

Tran H, Hamada F, Schwarz-Romond T, Bienz M. 2008. Trabid, a new positive regulator of Wnt-induced transcription with preference for binding and cleaving K63-linked ubiquitin chains. *Genes Dev* **22**: 528-542.

Tran H, Polakis P. 2012. Reversible modification of adenomatous polyposis coli (APC) with K63-linked polyubiquitin regulates the assembly and activity of the beta-catenin destruction complex. *J Biol Chem* **287**: 28552-28563.

Vaughan N, Scholz N, Lindon C, Licchesi JDF. 2022. The E3 ubiquitin ligase HECTD1 contributes to cell proliferation through an effect on mitosis. *Sci Rep* **12**: 13160.

Vega-Lopez GA, Cerrizuela S, Tribulo C, Aybar MJ. 2018. Neurocristopathies: New insights 150 years after the neural crest discovery. *Dev Biol* **444 Suppl 1**: S110-S143.

Yokota Y, Kim WY, Chen Y, Wang X, Stanco A, Komuro Y, Snider W, Anton ES. 2009. The adenomatous polyposis coli protein is an essential regulator of radial glial polarity and construction of the cerebral cortex. *Neuron* **61**: 42-56.

Yu Y, Zheng Q, Erramilli SK, Pan M, Park S, Xie Y, Li J, Fei J, Kossiakoff AA, Liu L et al. 2021. K29-linked ubiquitin signaling regulates proteotoxic stress response and cell cycle. *Nat Chem Biol* **17**: 896-905.

Yuan WC, Lee YR, Lin SY, Chang LY, Tan YP, Hung CC, Kuo JC, Liu CH, Lin MY, Xu M et al. 2014. K33-Linked Polyubiquitination of Coronin 7 by Cul3-KLHL20 Ubiquitin E3 Ligase Regulates Protein Trafficking. *Mol Cell* **54**: 586-600.

Figures

Figure 1

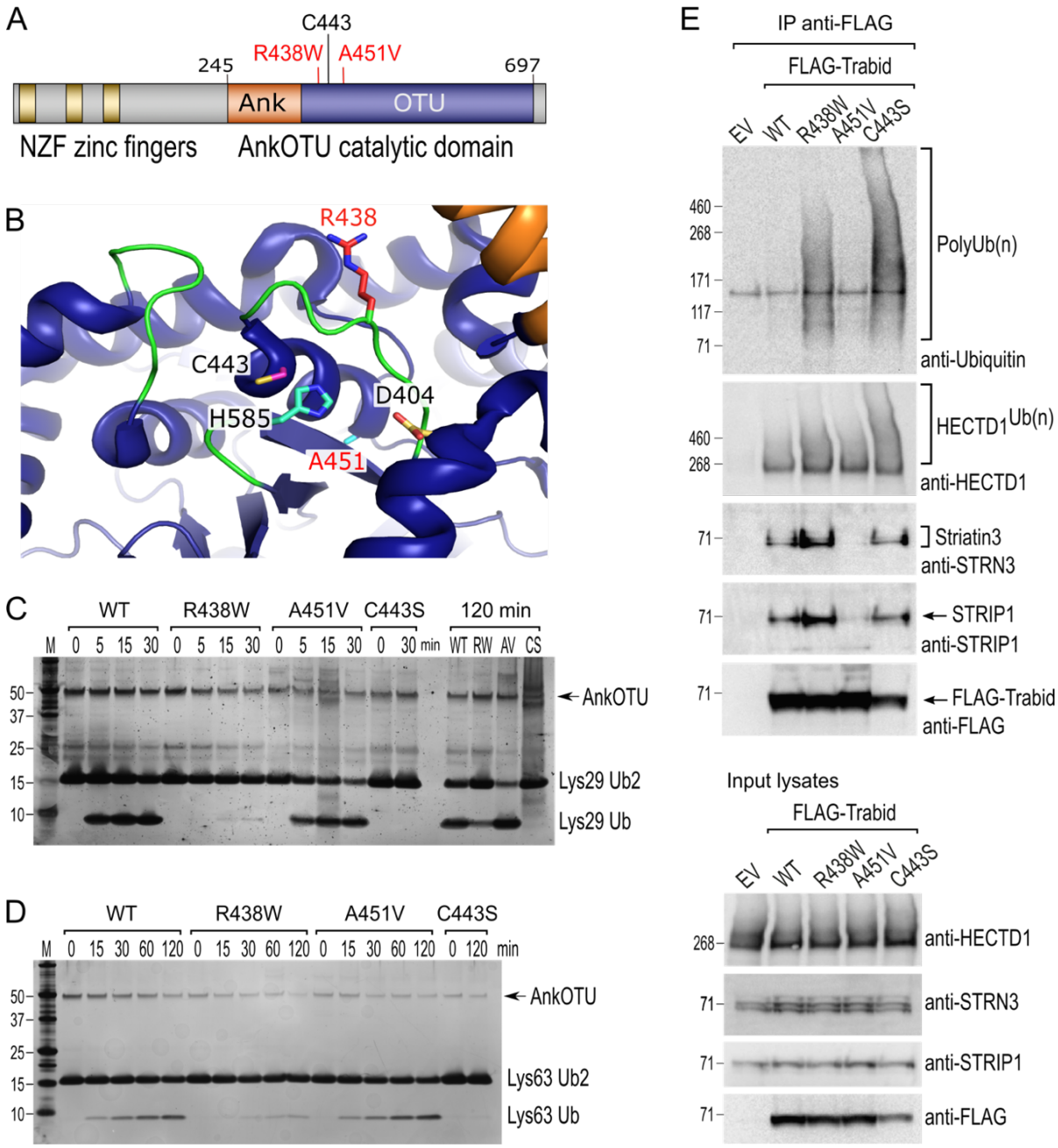

Figure 1. Trabid patient mutants are impaired in DUB activity and STRIPAK binding.

A. Trabid patient mutations R438W and A451V flank either side of the catalytic cysteine C443 in Trabid's AnkOTU domain.

B. Residue R438 project prominently into the catalytic cleft formed by the Ank and OTU domain, whereas residue A451 reside at the back of the active site. The positions of the catalytic triad residues C443, H585 and D404 are shown. Crystal structure of AnkOTU domain: PDB 3ZRH.

C and **D**. *In vitro* DUB assays. Hydrolysis of Lys29-linked (C) and Lys63-linked (D) di-ubiquitin chains by purified wild-type and mutant Trabid AnkOTU proteins. The Trabid R438W AnkOTU domain exhibit strongly reduced DUB activity M, molecular weight markers in kilodaltons.

E. Immunoprecipitation of FLAG-Trabid from the lysates of transfected HEK293T cells showed that FLAG-Trabid R438W and C443S mutants co-precipitated high amounts of endogenous polyubiquitin (PolyUb(n) smear), indicating impaired DUB activity. FLAG-Trabid A451V failed to efficiently co-precipitate Striatin3 and STRIP1, indicating loss of binding to the STRIPAK complex. All FLAG-Trabid proteins co-precipitated similar amounts of the E3 ubiquitin ligase HECTD1. EV, empty vector control.

Figure 2

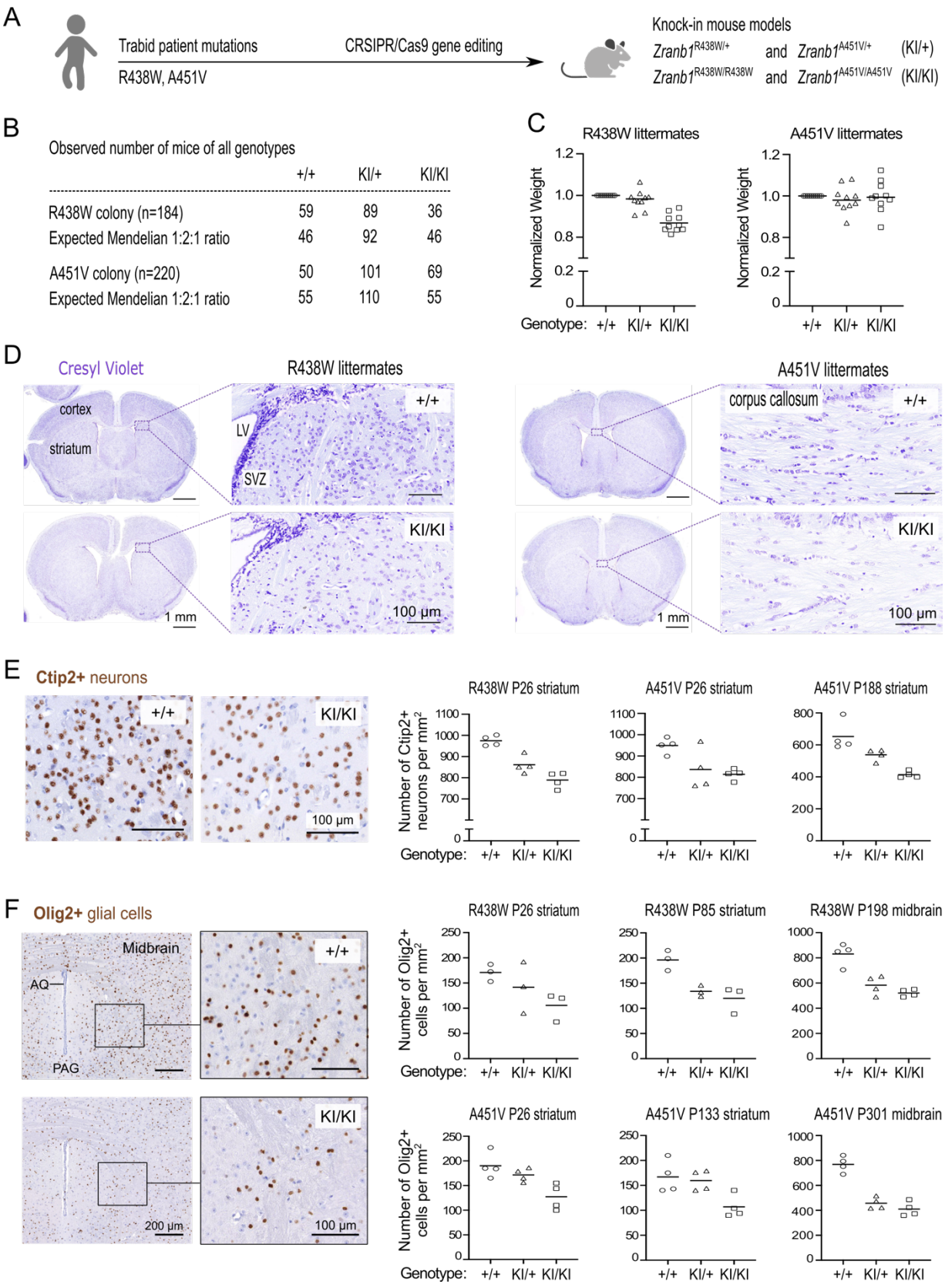

740

Figure 2. Decreased cell density in the brains of mice harbouring Trabid patient mutations.

A. Schematic of knock-in mouse strains harbouring *Zranb1/Trabid* patient mutations generated by CRISPR/Cas9 genome editing.

B. Numbers of mice of all genotypes produced from heterozygous intercrosses in the R438W or A451V colony, respectively.

C. Normalized weight of 10 sets of weaned littermate mice (5 males, 5 females; age range P26-P222) from each Trabid mutant colony. For each set of littermates, the weight of the wild-type (+/+) mouse was set at 1 and the weight of KI/+ or KI/KI mutant mice expressed as a ratio of the wild-type mouse weight.

D. Coronal brain sections (Bregma ±0.3mm) of weaned (postnatal day P26) littermate males from the R438W and A451V mouse colonies were stained with Cresyl Violet to assess general anatomy and cellular organisation in the cerebral cortex and striatum. LV, lateral ventricle; SVZ, subventricular zone. An overall decrease in Cresyl Violet staining intensity was evident in mutant homozygous (KI/KI) sections from both mouse strains compared to similar sections from the respective wild-type (+/+) littermate.

E. Ctip2 IHC revealed reduced numbers of medium spiny neurons in the striatum of mutant mice from the R438W and A451V colonies compared to wild-type littermate mice. Representative images shown are coronal brain sections of P26 male littermates from the R438W colony. Each data point represents the cell count in a randomly selected, non-overlapping 1 mm square area in the striatum from both brain hemispheres. The age and brain region of the cell count for 3 sets of littermate mice from the indicated mutant strain are specified. Cell numbers were quantified blinded to genotype using images processed in Fiji software. See Supplementary Figure 2.

F. Olig2 IHC revealed reduced numbers of oligodendrocytes in the striatum and midbrain of homozygous mice from the R438W and A451V colonies compared to respective wild-type littermates. Representative images shown are coronal sections from the ventral midbrain of P301 female littermates from the A451V colony (AQ, cerebral aqueduct; PAQ, periaqueductal gray). Each data point represents the cell count in a randomly selected, non-overlapping 1 mm square area in the striatum or midbrain from both brain hemispheres. The age and brain region of the cell count for 3 sets of littermate mice from the indicated mutant strain are specified. Cell numbers were quantified blinded to genotype using images processed in Fiji. See Supplementary Figure 2.

Figure 3

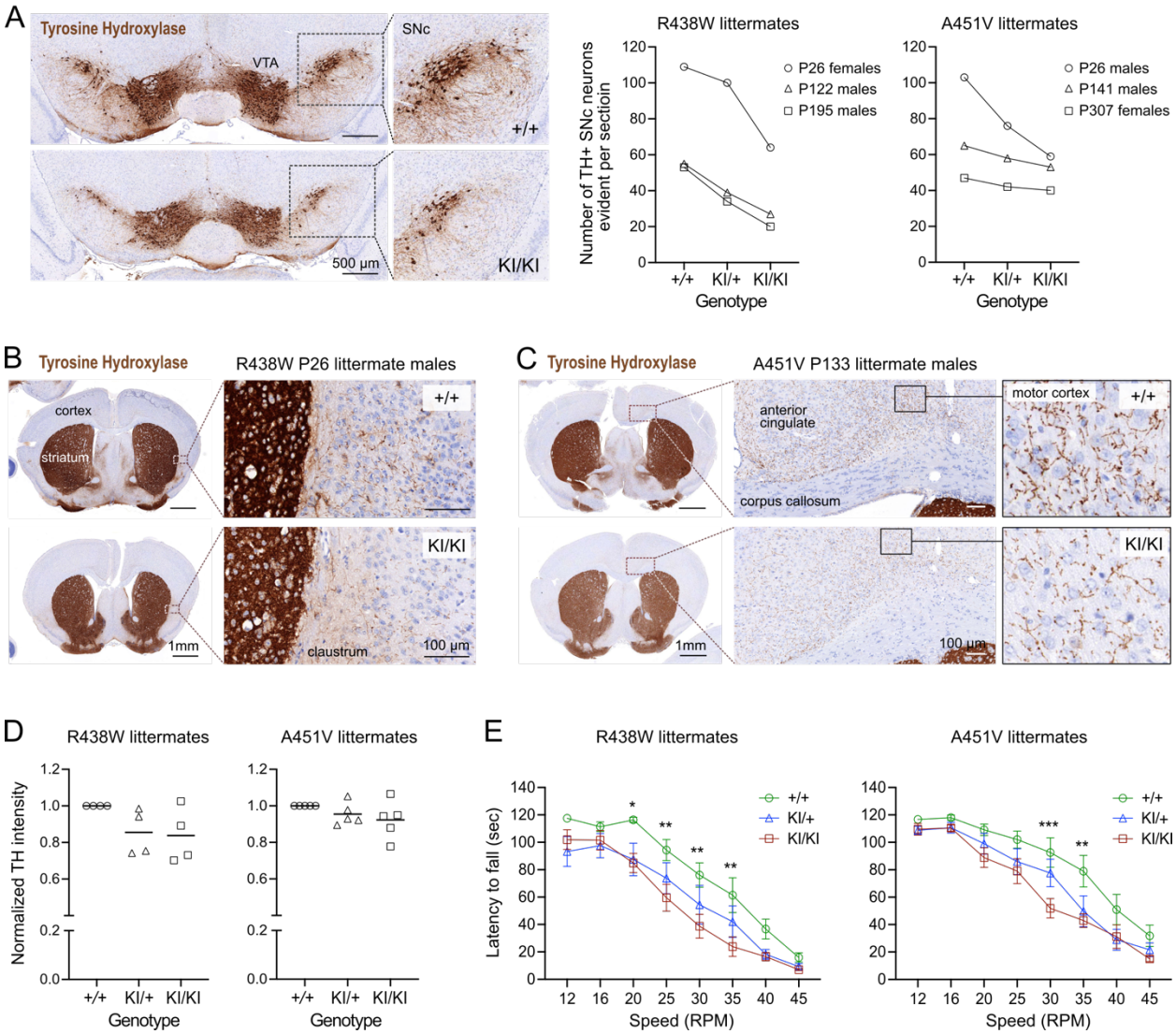

Figure 3. Trabid mutant mice exhibit a motor deficit consistent with reduced numbers of dopaminergic neurons and projections.

A. Tyrosine Hydroxylase (TH) IHC of coronal midbrain sections revealed reduced numbers of TH+ dopaminergic neurons in the substantia nigra pars compacta (SNc) of homozygous mutant mice from the Trabid R438W and A451V colonies compared to similar midbrain sections of the respective wild-type littermates. Representative images shown are midbrain sections of P26 female littermates from the R438W colony. VTA, ventral tegmental area. Numbers of TH+ SNc neurons were quantified using IHC images processed in Fiji. See Supplementary Figure 2.

B. Tyrosine Hydroxylase IHC of coronal brain sections (Bregma ±0.3mm) of P26 littermate mice from the Trabid R438W colony revealed reduced TH staining intensity in the striatum and fewer TH+ projections in the adjacent cortex of homozygous mutant mice compared to similar regions in the wild-type littermate (magnified area).

C. Tyrosine Hydroxylase IHC of coronal brain sections (Bregma ±0.3mm) of P133 littermate mice from the Trabid A451V colony revealed reduced abundance and intensity of TH+ projections in several cortical regions including the primary/secondary motor cortex of homozygous mutant mice compared to similar regions in the wild-type littermate (magnified area).

D. Tyrosine Hydroxylase staining intensity in the striatum of mutant mice from the R438W and A451V colonies normalized to the staining intensity of wild-type littermate sections. IHC signals were measured as the optical density of the region of interest demarcated manually using Fiji. Each symbol represents one mouse of the indicated genotype belonging to a set of littermate mice from the R438W colony (n=4 sets: P26 males, P93 females, P307 males, P480 females) or the A451V colony (n=5 sets: P26 males, P41 females, P133 males, P188 females, P303 females).

E. Rotarod performance of 3 to 4-month-old littermate mice from the R438W and A451V colonies. Each data point represents the average latencies of 8 mice (4 males, 4 females), where each mouse was subjected to 6 trials over 3 days. Wild-type (+/+), heterozygous (KI/+) and homozygous (KI/KI) littermate mice were tested together. The experimenter was blinded to genotype. A repeated measures two-way ANOVA and Dunnett's multiple comparisons test was applied to the data, using wild-type mice as the control group. Asterisks denote statistically significant differences between wild-type (+/+) and homozygous (KI/KI) mutant mice. *$p<0.05$, **$p<0.01$, ***$p<0.001$. Error bars, ±SEM.

Figure 4

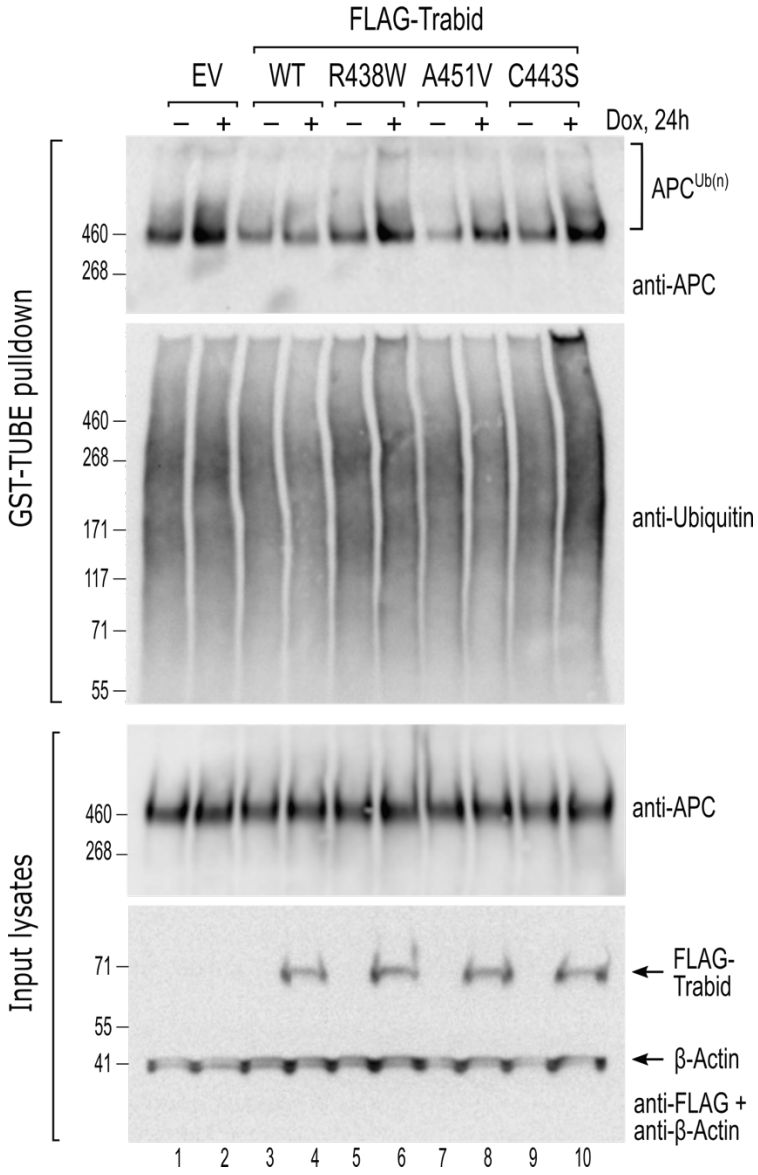

Figure 4. Trabid patient mutants fail to efficiently suppress APC ubiquitylation in cells. HEK293 cells stably transfected with doxycycline inducible constructs for the expression of wild-type or mutant FLAG-Trabid were untreated (-) or treated with dox (+; 100 ng/ml) for 24h. Cell lysates were subjected to a GST-TUBE pulldown to enrich the ubiquitylated proteome. Precipitated material and input lysates were processed for Western blotting using the indicated antibodies. Endogenous APC protein levels remained unchanged irrespective of FLAG-Trabid expression (input lysates), but ubiquitylated APC species were only efficiently suppressed by wild-type FLAG-Trabid expression ($APC^{Ub(n)}$; WT +). EV, empty vector control.

Figure 5

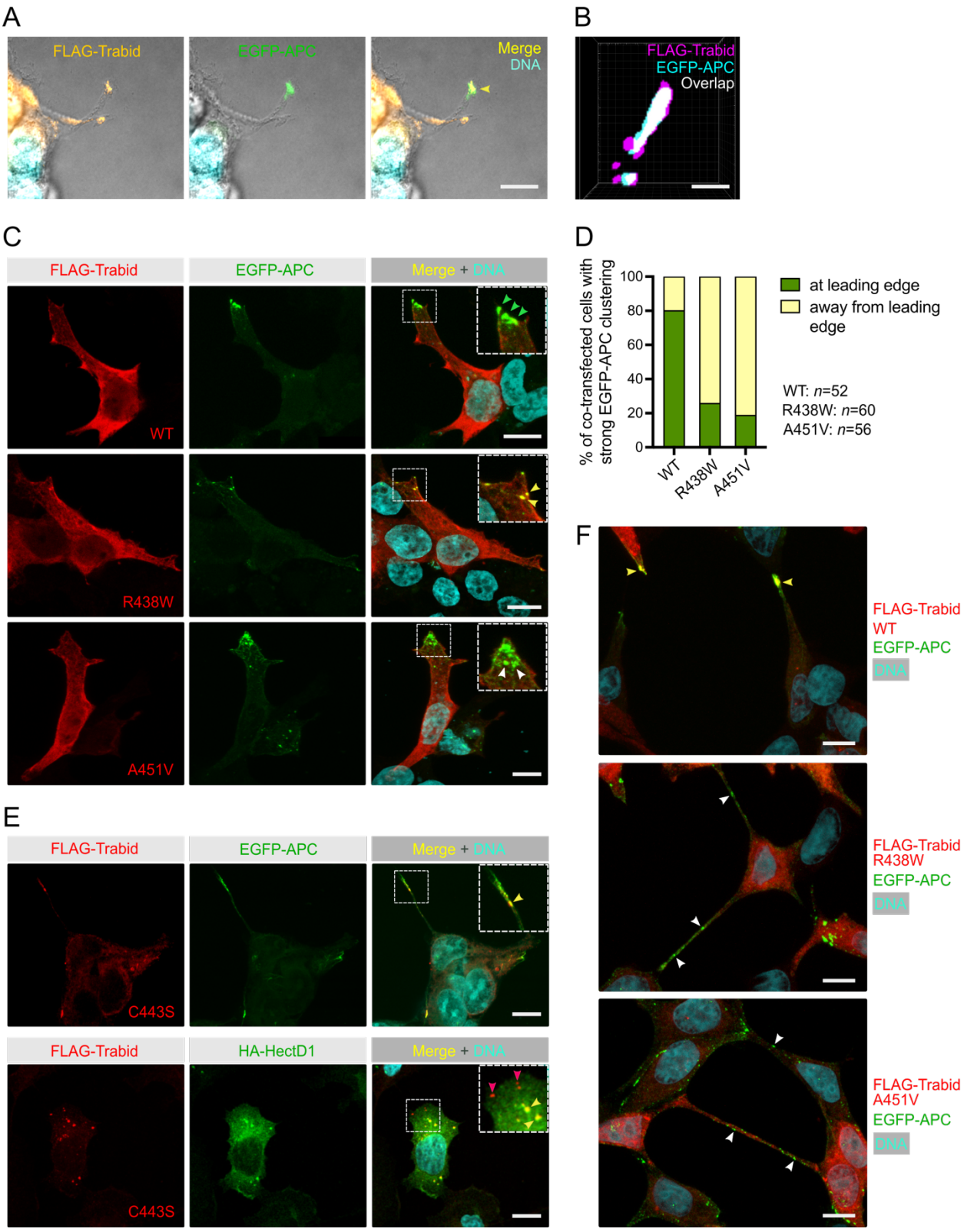

822

Figure 5. Trabid patient mutants impede the transport of EGFP-APC to the leading edge of migrating cells.

A. Combined differential interference contrast and immunofluorescence images of HEK293T cells extending long cell processes that contain FLAG-Trabid and EGFP-APC in the cortical protrusions of co-transfected cells (arrowhead in merged image). Scale bar, 10 μm.

B. 3D-SIM super resolution microscopy analysis of HEK293T cell tip clusters (n=5) revealed ~30% overlap of FLAG-Trabid and EGFP-APC signals at resolutions of ~100 nm in *xy* and 320 nm in *z*. Scale bar, 100 nm.

C. EGFP-APC membrane clusters at the leading edge of migrating HEK293T cells (green arrowheads) are readily detected with FLAG-Trabid wild-type co-expression. In cells expressing FLAG-Trabid patient mutants, EGFP-APC aggregate in punctate structures near the leading edge (white arrowheads), that are often sequestered together with the FLAG-Trabid R438W mutant (yellow arrowheads). Scale bar, 10 μm.

D. Quantification of strong EGFP-APC clustering at or away from the leading edge membrane of co-transfected HEK293T cells, as shown in C. Numbers of cells analysed from 3 independent transfections are shown.

E. In co-transfected HEK293T cells, DUB-dead FLAG-Trabid C443S form puncta that sequesters EGFP-APC near the tips of long cell protrusions or sequesters HA-HECTD1 in the cytoplasm (yellow arrowheads). Notably, HA-HECTD1 was not detected in FLAG-Trabid C443S puncta that form near the leading edge membrane of migrating cells (red arrowheads). Scale bar, 10 μm.

F. In near-confluent HEK293T cells 48h post transfection, FLAG-Trabid patient mutants induce long thin tubes that connect neigbouring cells and extensive EGFP-APC aggregations are conspicuous along these tubular structures. This phenomenon was not observed in cells transfected with wild-type FLAG-Trabid. Scale bar, 10 μm.

Figure 6

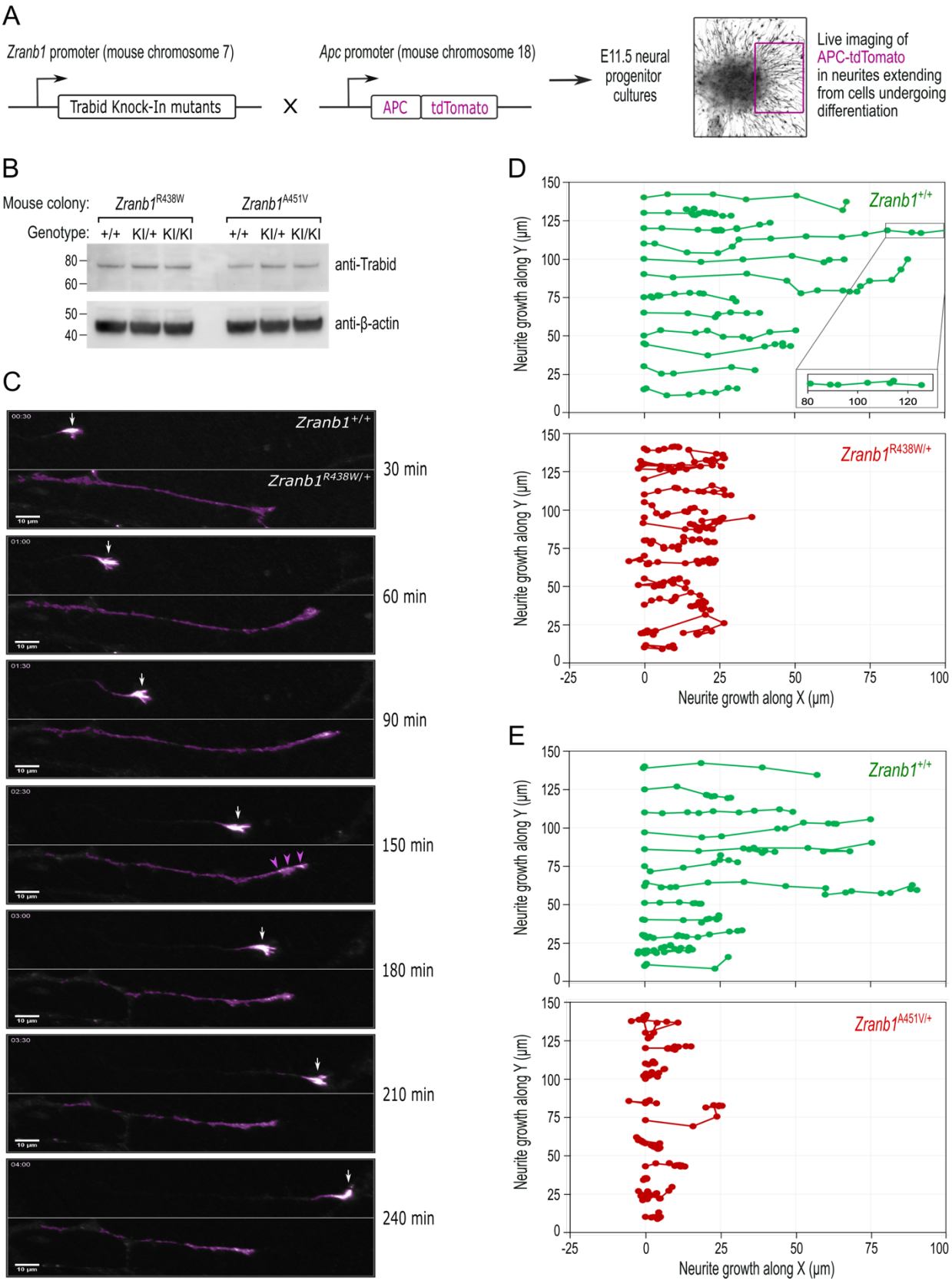

853

Figure 6. Trabid patient mutations perturb the trafficking of APC-tdTomato and the trajectory of neurite outgrowth.

A. Schematic of outcross between knock-in mice harbouring *Zranb1/Trabid* patient mutations and $Apc^{tdTomato}$ mice, where the APC-tdTomato fluorescent protein is expressed under the control of the endogenous *Apc* gene promoter. Midbrain neural progenitors derived from E11.5 embryos of these outcrosses were used for live cell imaging of APC-tdTomato trafficking in growing neurites.

B. Western blot analysis of Trabid protein expression in E11.5 midbrain neural progenitors derived from heterozygous intercrosses in the *Zranb1/Trabid* R438W or A451V mouse colonies. Mutant Trabid protein levels are expressed at comparable levels to wild-type Trabid protein (compare KI/KI to +/+).

C. Live cell imaging of APC-tdTomato in neurites extending from E11.5 midbrain neural progenitors of a $Zranb1^{R438W/+}$;$Apc^{tdTom/+}$ outcross. The frames shown are from a 4h time lapse portraying the movement of APC-tdTomato. APC-tdTomato accumulated in the tips of neurites with wild-type Trabid ($Zranb1^{+/+}$) to generate growth cones that drive axon elongation (white arrows). In neurons with mutant Trabid ($Zranb1^{R438W/+}$; $Zranb1^{A451V/+}$ data not shown), APC-tdTomato intensities were broadly distributed along neurites (purple arrowheads) and the formation of growth cones was abrogated. Scale bar, 10 μm.

D and **E**. The movement of Apc-tdTomato in individual neurite tips was tracked to visualize growth trajectory. Neurites extending from E11.5 midbrain neural progenitors of $Zranb1^{R438W/+}$;$Apc^{tdTom/+}$ (D) or $Zranb1^{A451V/+}$;$Apc^{tdTom/+}$ (E) outcrosses were analysed. Each data point represents the location of APC-tdTomato at 15-min intervals of a 4h time lapse. APC-tdTomato fluorescence synchronised with the movement of a membrane dye during neurite extension/retraction (data not shown) and was therefore used as a proxy for neurite growth along an arbitrary X and Y plane. Neurite tracking data were compiled from the imaging of neurite outgrowth in 3 independent neurosphere cultures established from E11.5 embryos of 3 independent $Zranb1^{R438W/+}$;$Apc^{tdTom/+}$ or $Zranb1^{A451V/+}$;$Apc^{tdTom/+}$ outcrosses. All image acquisition, processing and analyses were performed blinded to genotype.

Figure 7

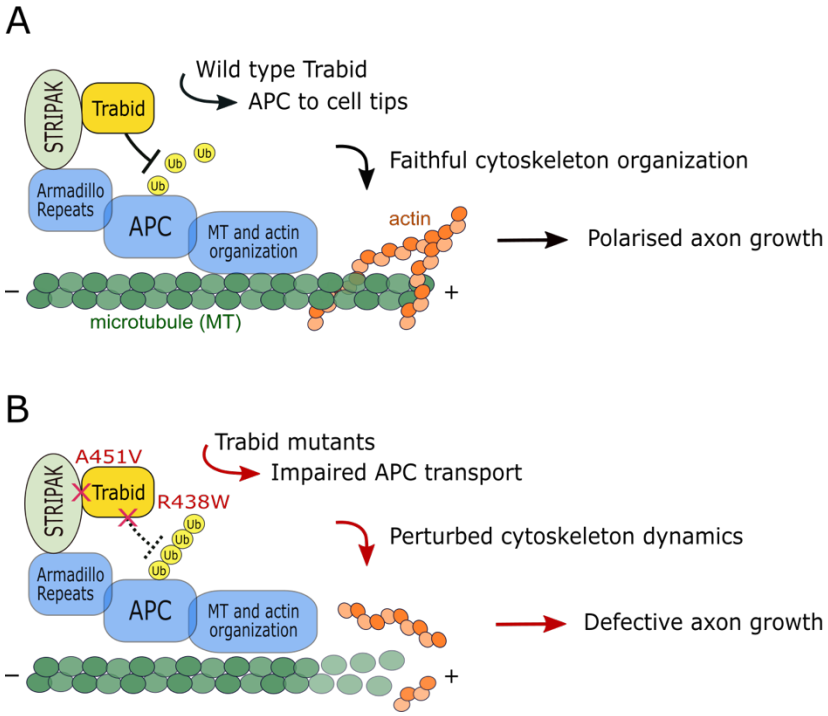

Figure 7. Model of Trabid's mechanism of action in axon growth and guidance.

A. STRIPAK recruits Trabid to deubiquitylate APC (and possibly other substrates). This promotes efficient APC accumulation at microtubule plus ends to coordinate the actin and microtubule cytoskeleton dynamics that drive directional cell migration and polarised axon growth.

B. In cells expressing Trabid mutants that are DUB-impaired (R438W) or STRIPAK-binding-deficient (A451V), APC becomes persistently modified with ubiquitin chains that retard its transport to cell tips. This impairs cytoskeleton organisation which leads to defective axon elongation and cell migration. Future studies will aim to identify the mechanism of Trabid recruitment to STRIPAK, the ubiquitin-modified residue(s) on APC (and possibly other substrates), and the composition of polyubiquitin linkages on substrates including the Lys29- and Lys33-linked atypical chain types preferentially targeted by Trabid.